Ceramics International 49 (2023) 403–412

Contents lists available at ScienceDirect

Ceramics International

journal homepage: www.elsevier.com/locate/ceramint

Near-infrared-shielding energy-saving borosilicate glass-ceramic window materials based on doping of defective tantalum tungsten oxide ($Ta_{0.3}W_{0.7}O_{2.85}$) nanocrystals

Guang Yang [a], Yongwei Liu [a], Chuanfan Yang [a], Fang Xia [b,**], Daming Hu [a], Yupeng Wu [c,***], Yaroslav Shpotyuk [d,e,****], Viktor Takats [f], Xiaoyan He [a,g,*]

[a] School of Materials Science and Engineering, Shanghai University, Shanghai, 200444, China
[b] Harry Butler Institute, Murdoch University, Perth, WA, 6150, Australia
[c] Department of Architecture and Built Environment, Faculty of Engineering, The University of Nottingham, University Park, Nottingham, NG7 2RD, United Kingdom
[d] Department of Sensor and Semiconductor Electronics, Ivan Franko National University of Lviv, 107 Tarnavskoho Str., 79017 Lviv, Ukraine
[e] Institute of Physics, University of Rzeszow, 1 Pigonia Str., 35-959, Rzeszow, Poland
[f] Institute for Nuclear Research, Hungarian Academy of Sciences, Debrecen, 4001, Hungary
[g] Editorial Office of Electrochemical Energy Reviews, Periodicals Agency of Shanghai University, Shanghai University, Shanghai, 200444, China

ARTICLE INFO

Keywords:
Defective tungsten oxide
NIR-Shielding
Energy-saving glass-ceramics
Tantalum doped
$Ta_{0.3}W_{0.7}O_{2.85}$

ABSTRACT

NIR-shielding window materials were fabricated by direct embedding of $Ta_{0.3}W_{0.7}O_{2.85}$ nanocrystals in bulk borosilicate glass-ceramics during a facile melt-quenching process. Optical and thermal performance of the prepared windows can be adjusted by varying the concentration of H_2WO_4 and Ta_2O_5 in the starting materials. The optimized window fabricated from raw materials containing 4.5 mol% H_2WO_4 and 0.3 mol% Ta_2O_5 exhibited high visible light transmittance 74.4% and strong NIR-shielding ability $\Delta T = 68.9\%$. Its thermal insulation performance is much better than soda lime glass or ITO glass, and its visible light transmission is higher than cesium-tungsten-bronze-based film coated glass. The distribution of $Ta_{0.3}W_{0.7}O_{2.85}$ functional nanocrystals in the glass matrix was confirmed by sample characterization using XRD, Raman, XPS, HRTEM and EDS. The NIR-shielding property has been attributed to local surface plasmon resonance due to oxygen vacancies in the $Ta_{0.3}W_{0.7}O_{2.85}$ nanocrystals. This study sheds a light on fabricating energy-saving windows with a tunable NIR-shielding performance.

1. Introduction

Energy-saving technologies are becoming urgently important for coping worsening global warming and climate change problems. This is because today's world is still heavily relying on fossil fuel-based energy sources. One of the effective energy-saving technologies is energy-saving building windows. Annually, about 40% of total global energy is consumed in buildings [1], and up to 40% of building energy consumption is due to heat transfer through glass windows [2,3]. These glasses can effectively transmit visible light, but they also bring sunlight heat into the building due to their high transmission of near infrared (NIR) light [4,5]. The transmitted NIR light raises room temperature, and the regulation of temperature requires excessive utilization of air conditioners [2]. The reduction of building energy consumption can be achieved by the application of energy-saving windows because these windows offer both excellent visible light transmission and excellent NIR-shielding ability [6].

NIR-shielding film-based glass windows have been widely applied for thermal insulation against sunlight thermal irradiation. NIR-shielding films have been developed based on vanadium oxide (VO_2)

* Corresponding author. School of Materials Science and Engineering, Shanghai University, Shanghai, 200444, China.
** Corresponding author. Harry Butler Institute, Murdoch University, Perth, WA, 6150, Australia.
*** Corresponding author. Department of Architecture and Built Environment, Faculty of Engineering, The University of Nottingham, University Park, Nottingham, NG7 2RD, United Kingdom.
**** Corresponding author. Department of Sensor and Semiconductor Electronics, Ivan Franko National University of Lviv, 107 Tarnavskoho Str., 79017 Lviv, Ukraine.
E-mail addresses: f.xia@murdoch.edu.au (F. Xia), Yupeng.Wu@nottingham.ac.uk (Y. Wu), yshpotyuk@ur.edu.pl (Y. Shpotyuk), jialete592@i.shu.edu.cn (X. He).

https://doi.org/10.1016/j.ceramint.2022.09.003
Received 20 July 2022; Received in revised form 24 August 2022; Accepted 1 September 2022
Available online 6 September 2022

Table 1
The nominal compositions of the prepared bulk glass and glass-ceramic samples.

Sample name	Nominal compositions of the raw materials (mole %)				
	H_2WO_4	SiO_2	B_2O_3	NaF	Ta_2O_5
4.5W0Ta	4.50	27.70	41.07	26.74	0
4.5W0.2Ta	4.50	27.64	40.98	26.68	0.20
4.5W0.3Ta	4.50	27.61	40.94	26.66	0.30
4.5W0.4Ta	4.50	27.58	40.89	26.63	0.40
4.5W0.5Ta	4.50	27.55	40.85	26.60	0.50
3.5W0.3Ta	3.50	27.90	41.37	26.94	0.30
4W0.3Ta	4.00	27.75	41.15	26.80	0.30
5W0.3Ta	5.00	27.46	40.72	26.52	0.30
5.5W0.3Ta	5.50	27.32	40.51	26.38	0.30

[7,8], indium-doped tin oxide (ITO) [9], antimony-doped tin oxide (ATO) [10], and tungsten bronze [11–13]. In addition, energy-saving films with high long-wave infrared (LWIR) emissivity can also decrease indoor temperature by radiating LWIR to the outer space. For example, Wang et al. prepared thermochromic smart films with passive LWIR radiative cooling regulation [14,15]. However, these functional films on glass panels are prone to degradation and peeling when they are subjected to strong UV radiation or scratches [16], and are difficult to be applied on complex-shaped glass surfaces.

Recent research has shown that NIR-shielding functional units M_xWO_3 can be introduced directly into the bulk glass matrix by the melt-quenching glass fabrication technique [12,17]. This technique omits the requirement of functional film on glass, and hence the lifespan of the glasses can be significantly enhanced. The NIR-shielding performance of these glasses can be fine turned by adjusting the concentration of the reduced tungsten oxide (WO_{3-x}) or the type of alkali metals (Li^+, Na^+, K^+), and the resulting NIR-shielding performance is comparable to film-based glasses [12,17,18]. The challenges of this technique include the requirement of maintaining a reducing atmosphere during the glass fabrication process in order to form W^{5+} in WO_{3-x}, and the low visible light transmission below 65% due to high concentration of amorphous M_xWO_3 functional units [19]. To improve visible light transmission and maintain strong NIR absorption, it is required to dope smaller amount of functional units with better NIR-shielding property. Compared with amorphous M_xWO_3 functional units, fine nanocrystal functional units such as nano rod defective oxide crystals are usually more effective in NIR-shielding [20,21].

Defective tungsten oxide (WO_{3-x}, $0 < x < 1$) exabits strong NIR-shielding ability because oxygen defects in WO_{3-x} can induce local surface plasmon resonance (LSPR) [19,22]. Generally, the LSPR effect is enhanced with increasing oxygen detects, and indeed highly defective $WO_{2.72}$ has been applied as a functional phase in energy-saving NIR--shielding film glasses [23]. Not surprisingly, $WO_{2.72}$ nanorods dispersed film has shown better thermal insulation than ITO glass under halogen lamp irradiation [21,24]. However, $WO_{2.72}$ is easily oxidized in air, causing gradual deterioration of NIR-shielding performance of $WO_{2.72}$ doped film [25]. This problem may be solved by doping transition metal ions into tungsten oxide such that the doping ions have a chemical state lower than W^{6+}, such as Nb^{5+} [26], Mo^{5+} [27], Ta^{5+} [28], Ti^{4+} [29] and Zn^{4+} [30]. For example, $Ta_{0.3}W_{0.7}O_{2.85}$ has shown excellent NIR-shielding effect due to high density of oxygen defects in $Ta_{0.3}W_{0.7}O_{2.85}$. The material also exhibits excellent thermal stability at temperatures as high as 750 °C [31,32]. Locking the crystalline $Ta_{0.3}W_{0.7}O_{2.85}$ functional units into the glass matrix may produce highly stable NIR-shielding energy-saving windows but this has not been studied so far.

In this work, we prepared $Ta_{0.3}W_{0.7}O_{2.85}$ nanocrystal doped glass-ceramics by the facile melt-quenching technique. The NIR-shielding performance was optimized by adjusting the concentrations of Ta_2O_5 and H_2WO_4 as the Ta and W sources, respectively. The formation of functional nanocrystals $Ta_{0.3}W_{0.7}O_{2.85}$ in the glass matrix were studied by detailed sample characterization using X-ray diffraction (XRD), Raman spectroscopy, X-ray photoelectron spectroscopy (XPS), transmission electron microscopy (TEM), high resolution transmission electron microscopy (HRTEM) and energy dispersive spectrometer (EDS). The optimal sample exhibits excellent NIR-shielding ability, high visible light transmittance, and strong thermal insulation under Xeon lamp irradiation.

2. Experimental section

2.1. Materials

High-purity raw materials were used: tungstic acid (H_2WO_4, ≥99.7%, Aladdin), silica (SiO_2, ≥99.7%, Sinopharm Chemical Reagent Co., Ltd.), boron trioxide (B_2O_3, ≥99.8%, Sinopharm Chemical Reagent Co., Ltd.), sodium fluoride (NaF, ≥99.8%, Aladdin) and tantalum pentoxide (Ta_2O_5, ≥99.5%, Aladdin). All the chemicals were used as received.

White float window glass (soda lime glass) was purchased from China Luoyang Float Glass Group Co., Ltd. and ITO glass was purchased from Zhuhai Kaivo Optoelectronic Technology Co., Ltd. Cesium-tungsten-bronze-based film coated glass (CWO film glass) was fabricated. Cesium tungsten bronze (Cs_xWO_3, CWO) powder was purchased from Hangzhou Jikang New Material Co., Ltd. The powder was dispersed in resin-toluene mixed solution and painted on soda lime glass and dried, following the reported process [33].

2.2. Fabrication of glass, glass-ceramic, and ceramic samples

The bulk glasses or glass-ceramics were prepared using a facile melt-quenching technique under an air atmosphere, using the nominal compositions shown in Table 1. Powders of raw materials were uniformly mixed in a corundum crucible. Later, mixtures were heated to 600 °C and held for 2 h. Then the heated mixtures were melt in an elevator furnace at 1400 °C for 2 h. After that, the melts were cooled to 1100 °C for clarification, and poured into a graphite mold for quenching and solidification. Finally, the solidified samples were annealed at 450 °C for 6 h. The prepared samples were cut into pieces with a thickness of 5 mm, and double-side polished. They were named as xWyTa, meaning the sample was prepared using x mol% of H_2WO_4 and y mol% of Ta_2O_5. For instance, 4.5W0.3Ta means the sample was prepared using 4.5 mol% of H_2WO_4 and 0.3 mol% of Ta_2O_5.

To study the structure of the bulk glass and glass-ceramic samples, ceramic powders were prepared by heating bulk glasses and glass-ceramics at 700 °C for 12 h in a tube furnace under N_2 atmosphere with a flow rate of 400 mL min^{-1}. The ceramic powders were named using a suffix C after the name of the corresponding bulk glass or glass-ceramics, such as 4.5W0.3Ta–C.

2.3. Material and device characterization

A UV–Vis–NIR spectrophotometer (UH4150, Hitachi, Tokyo, Japan) was used to record the transmittance spectra of the samples. Raman spectra were obtained by a laser micro-Raman spectrometer (inVia Qontor, Renishaw, Britain) with an excitation wavelength of 532 nm. Crystalline phases were identified by XRD (D/MAX-2500V/PC, Rigaku, Japan) with a Cu-Kα radiation (λ = 1.5418 Å). The valance states of W were determined by XPS (Thermo Scientific K-Alpha+, Thermo Fisher, USA). The morphology and distribution of the functional nanocrystals in energy-saving samples and ceramic powders were examined by TEM (F200X G2, FEI, USA). The element distributions in the samples were determined by EDS (Super-X, FEI, USA).

2.4. Simulation test

The thermal insulation performance of the window samples was tested in a simulated thermal insulation chamber with a dimension of 10

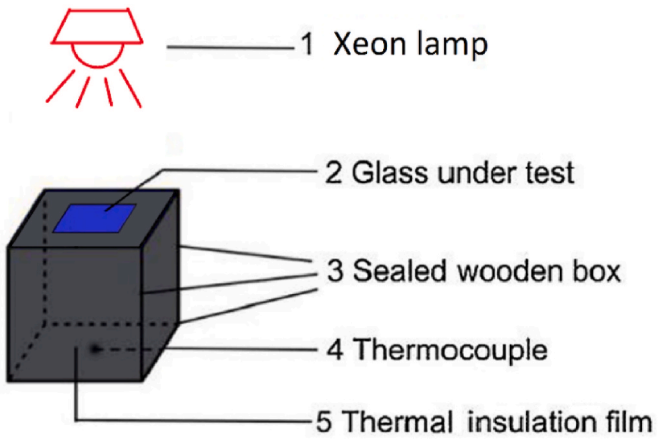

Fig. 1. Schematic diagram of the thermal insulation simulation chamber: the thermal insulation effect of soda lime glass, ITO glass, CWO film glass, and 4.5W0.3Ta glass-ceramic were tested, respectively.

× 10 × 10 cm^3 (Fig. 1). The chamber was made of wooden plates and insulated by wrapping with Styrofoam and aluminum foil. A transparent window with a dimension of 4 × 4 cm was installed on the top of chamber and was covered by four types of windows (ITO glass, CWO film glass, soda lime glass and 4.5W0.3Ta glass-ceramic), respectively. The chamber was irradiated by a Xeon lamp with light power density of 1000 W/m^2, because a Xeon lamp has similar spectral energy distribution as sunlight. The temperature inside the chamber was recorded in every 10 s with a thermometer.

3. Results and discussion

3.1. Optical property of the samples

The UV–Vis–NIR transmittance spectra of the samples and the variation of optical performance parameters (ΔT and T_{max}) as a function of Ta_2O_5 and H_2WO_4 concentrations are shown in Fig. 2. Here ΔT is defined as the difference between the maximum visible light transmission and the minimum NIR transmission between 300 nm and 2100 nm and is used to quantify the NIR-shielding ability, while T_{max} is defined as the highest transmittance in the spectra and is used to indicate visible transparency of the sample.

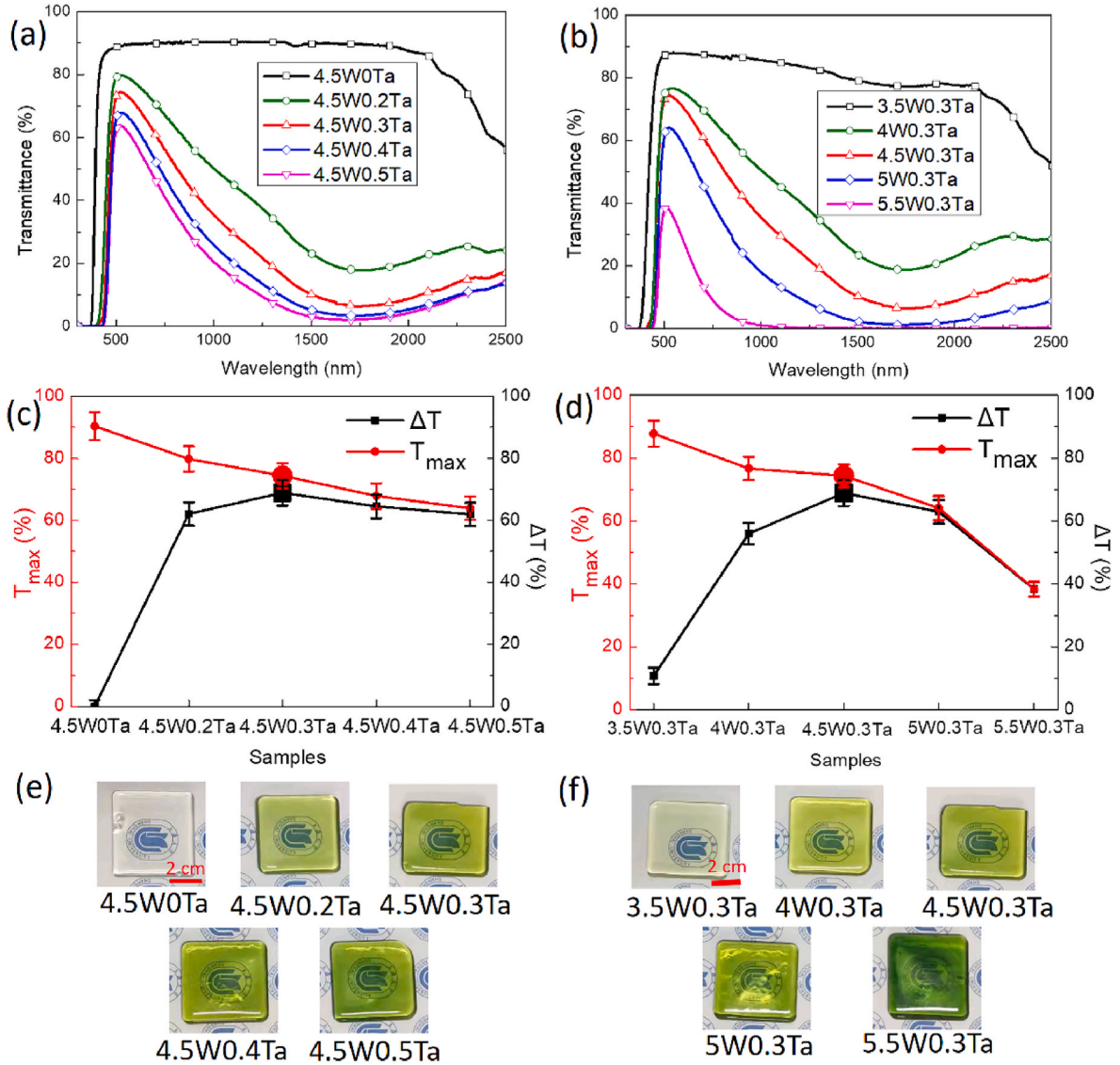

Fig. 2. UV–Vis–NIR transmission spectra (a, b), ΔT and T_{max} (c, d), and photos (e, f) of the samples as a function of Ta_2O_5 and H_2WO_4 concentration.

Table 2
The NIR-shielding properties of different types of samples (6WO-1, 5W1.25Sb, 6W, 4.5W0.3Ta) [17,35,36].

	6WO-1	5W1.25Sb	6W	4.5W0.3Ta
ΔT	59.1%	62.8%	64.1%	68.9%
T_{max}	63.9%	67.7%	71.0%	74.4%

Fig. 2(a, c, e) show the effect of Ta_2O_5 concentration on the optical properties of the samples. The results suggest that sample 4.5W0Ta with no Ta_2O_5 does not shield NIR while sample 4.5W0.5Ta with the highest amount of Ta_2O_5 has excellent NIR-shielding effect (ΔT = 62.0%). The tradeoff for NIR-shielding is the deterioration in visible light transmission, with sample 4.5W0.5Ta showing the lowest visible light transmittance (T_{max} = 63.9%), likely due to excessive NIR-shielding function phase. Accordingly, with increasing content of Ta_2O_5, the color of the samples deepens from milky (4.5W0Ta) to yellow (4.5W0.2Ta), greenish yellow (4.5W0.3Ta and 4.5W0.4Ta) and dark green (4.5W0.5Ta) as shown in Fig. 2(e).

Fig. 2(b, d) show the effect of H_2WO_4 concentration on the optical properties of the samples. Similarly, the results suggest that sample 3.5W0.3Ta with the least amount of H_2WO_4 shows little NIR-shielding ability (ΔT = 10.7%) while sample 5.5W0.3Ta with the highest amount of H_2WO_4 is least transparent (T_{max} = 38.3%) due to excessive NIR-shielding function phase. This agrees with deepening sample color with increasing H_2WO_4 content, from milky (3.5W0.3Ta) to yellow (4W0.3Ta), greenish yellow (4.5W0.3Ta and 5W0.3Ta), and dark green (5.5W0.3Ta) as shown in Fig. 2(f).

The above results conclude that the introduction of Ta_2O_5 and H_2WO_4 favor the formation of NIR-shielding functional phase but too much Ta_2O_5 and H_2WO_4 deteriorates visible light transmittance. The optimal sample is 4.5W0.3Ta which has the best NIR-shielding ability (ΔT = 68.9%) and high visible light transmittance (T_{max} = 74.4%). These optical parameters are much better than the recently reported values for excellent NIR-shielding energy saving window materials such as $(K_{0.2}Cs_{0.8})_xWO_3$ films (ΔT = 65.1%, T_{max} = 66.9%) [34]. What's more, as shown in Table 2, 4.5W0.3Ta shows the best NIR-shielding performance compared with 6WO-1 (ΔT = 59.1%, T_{max} = 63.9%), 5W1.25Sb (ΔT = 62.8%, T_{max} = 67.7%) and 6W (ΔT = 64.1%, T_{max} = 71.0%) [17,35,36].

To further assess the optical transmission properties of the optimal sample 4.5W0.3Ta, solar irradiance transmittance in the visible region (T_{lum}, 380–780 nm) and total solar (T_{sol}, 300–2500 nm) were obtained according to the following equation:

$$T_{sol/lum} = \frac{\int T(\lambda)\varphi(\lambda)d\lambda}{\int \varphi(\lambda)d\lambda} \quad (1)$$

where T(λ) is the transmittance at wavelength λ and φ(λ) is the solar irradiance at 1.5 air mass according to the Standard Tables of ASTM G173-03. The optimal sample 4.5W0.3Ta has T_{lum} = 69.0% and T_{sol} = 42.4%, very close to the values of the recently reported NIR-shielding energy-saving Cs_xWO_3/PMMA composite material (T_{lum} = 70.0%, T_{sol} = 43.4%) [37].

3.2. Thermal insulation property of the samples

Thermal insulation performance of the optimal sample 4.5W0.3Ta

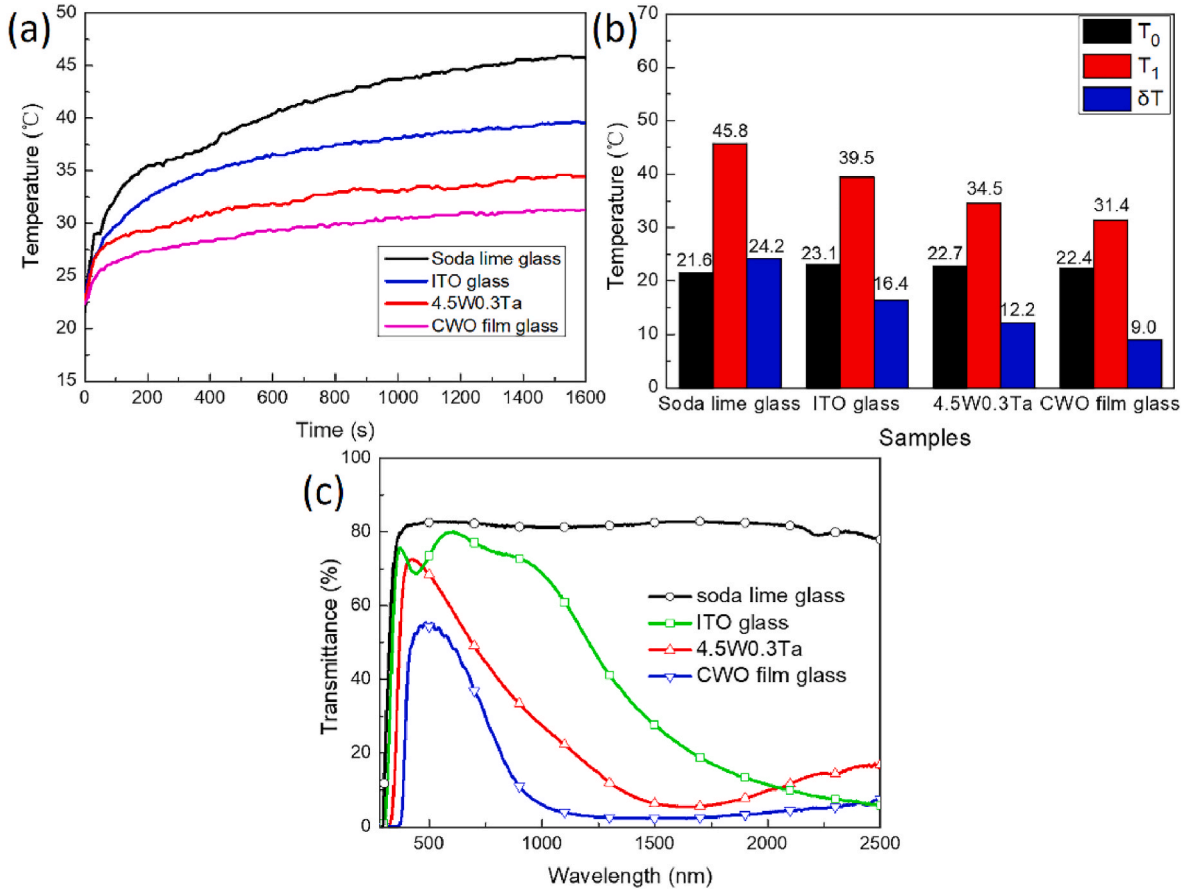

Fig. 3. (a) Temperature variations in the test chamber during 30 min irradiation under a xenon lamp, using soda lime glass, ITO glass, CWO film glass and 4.5W0.3Ta sample as windows. (b) Initial temperature, final temperature, and temperature difference in the simulated thermal insulation chambers, and (c) UV–Vis–NIR transmission spectra of the windows.

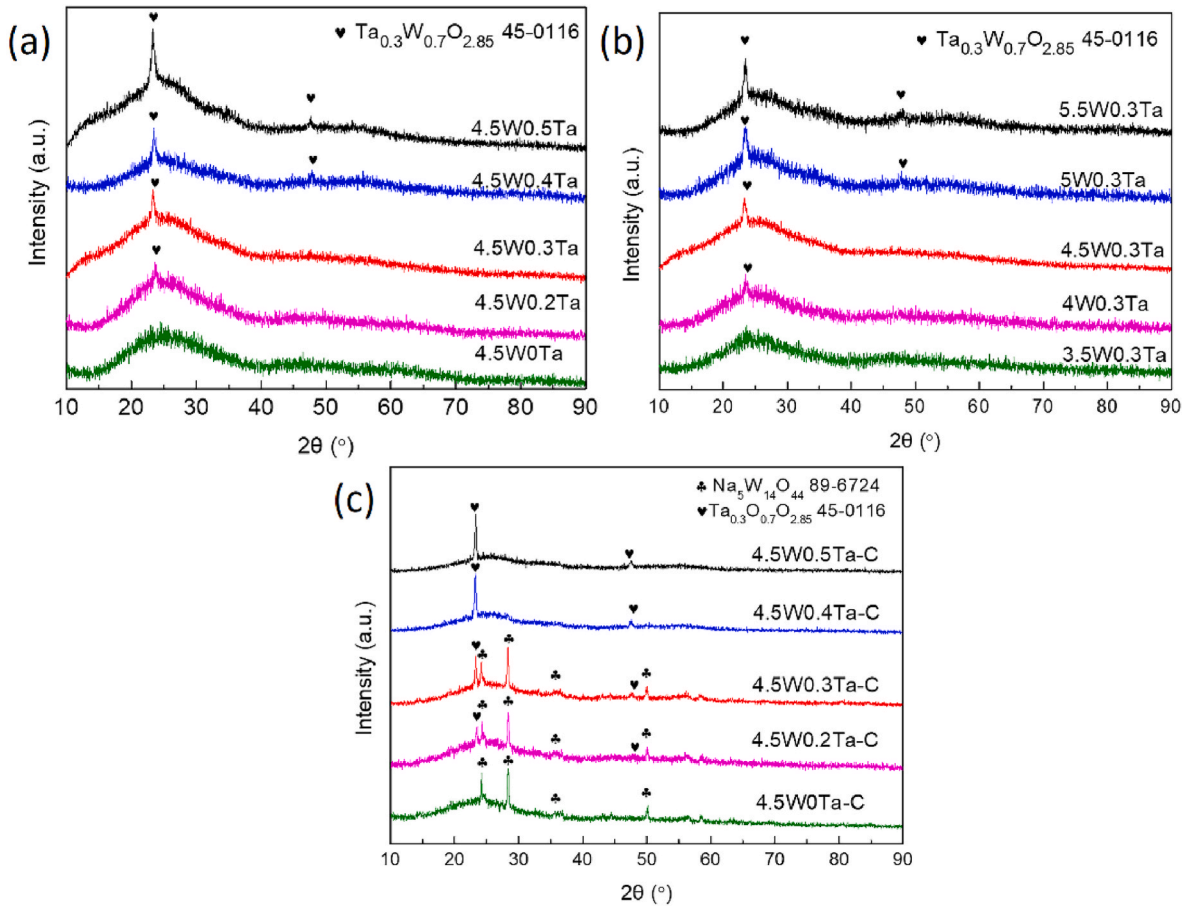

Fig. 4. XRD patterns of the samples as a function of (a) Ta_2O_5 and (b) H_2WO_4 concentration, respectively. (c) XRD patterns of ceramic samples produced by heat treatment of the glass samples at 700 °C for 12 h.

has been compared with that of CWO film glass, ITO glass and soda lime glass. The temperature variations during the simulated thermal insulation chamber tests are presented Fig. 3(a) and (b), where T_0, T_1, and δT are the initial temperature, final temperature, and temperature difference inside the testing chamber, respectively. After irradiation for 30 min, δT were 24.2 °C, 16.4 °C, 12.2 °C, and 9.0 °C for soda lime glass, ITO glass, 4.5W0.3Ta sample and CWO film glass, respectively (Fig. 3 (b)). This result agrees well with the UV–Vis–NIR transmittance spectra of these windows (Fig. 3(c)). Therefore, it can be concluded that sample 4.5W0.3Ta is able to shield more NIR light than ITO glass and soda lime glass. Sample 4.5W0.3Ta has slightly less NIR-shielding ability than CWO film glass, but its visible light transmittance (T_{max} = 74.4%) is 1.34 times higher than that of the CWO film glass (T_{max} = 55.5%) (Fig. 3(c)).

3.3. Origin of NIR-shielding performance

Evidence from XRD, TEM, EDS, Raman and XPS characterization of the samples suggest that the NIR-shielding effect is attributed to the formation of $Ta_{0.3}W_{0.7}O_{2.85}$ nanocrystals dispersed in the glass matrix. Fig. 4 (a) and (b) show that all samples except 4.5W0Ta and 3.5W0.3Ta show XRD diffraction peaks of $Ta_{0.3}W_{0.7}O_{2.85}$ (PDF: 45–0116). The peak at 23.5° can be assigned to diffraction from the (1 0 0) lattice planes of $Ta_{0.3}W_{0.7}O_{2.85}$ crystals. In samples 4.5W0.5Ta, 4.5W0.4Ta, 5.5W0.3Ta and 5W0.3Ta, another weak peak at 47.8° can be assigned to diffraction from the (2 0 0) lattice planes of $Ta_{0.3}W_{0.7}O_{2.85}$ crystal. These two diffraction peaks agree with XRD of reported $Ta_{0.3}W_{0.7}O_{2.85}$ crystal films [32,38].

To further confirm the functional units in the glass matrix, further crystal growth was induced by thermally treated the samples at 700 °C for 12 h under a nitrogen atmosphere. Except 4.5W0Ta–C which contains no Ta_2O_5, all other thermally treated samples showed the same but more intense two diffraction peaks at 23.5° and 47.8° (Fig. 4(c)), proving the presence of $Ta_{0.3}W_{0.7}O_{2.85}$ crystals in the samples. In samples 4.5W0.3Ta–C, 4.5W0.2Ta–C, and 4.5W0Ta–C with low the content of Ta_2O_5, $Na_5W_{14}O_{44}$ crystals were also present, and the phase abundance ratio of $Ta_{0.3}W_{0.7}O_{2.85}$ to $Na_5W_{14}O_{44}$ increased with increasing Ta_2O_5 content. This may suggest that a small amount of amorphous $Na_5W_{14}O_{44}$ was formed in the bulk samples due to insufficient Ta_2O_5 in the raw materials. It is worth noting that sample 4.5W0Ta–C shows the highest amount of $Na_5W_{14}O_{44}$ (Fig. 4(c)), yet it exhibits no NIR-shielding ability as indicated in the UV–Vis–NIR transmission spectrum (Fig. 2(a)). This suggests that effective functional units responsible for NIR-shielding in these samples is $Ta_{0.3}W_{0.7}O_{2.85}$ crystals but not amorphous $Na_5W_{14}O_{44}$.

The functional phase $Ta_{0.3}W_{0.7}O_{2.85}$ belong to a series of Ta_2O_5-doped WO_3, $Ta_xW_{1-x}O_{3-x/2}$, which were initially prepared and studied by Kudo et al. [31]. The crystal structure of $Ta_xW_{1-x}O_{3-x/2}$ is the same as stoichiometric WO_3, both belonging to the ReO_3-type crystal structure, and in $Ta_xW_{1-x}O_{3-x/2}$, the crystal structure is composed of corner shared [WO_6] octahedra and [TaO_6] octahedra. With increasing amount of Ta_2O_5 dopant, the concentration of oxygen vacancies within the crystal increases [31], based on the formation of defective $Ta_xW_{1-x}O_{3-x/2}$:

$$(1\text{-}x)WO_3 + x/2Ta_2O_5 \rightarrow Ta_xW_{1-x}O_{3-x/2} \quad (2)$$

In the ReO_3-type crystal structure, oxygen vacancies introduce free electron carriers. These electron carriers produce polarons because they are bound by W^{5+} and polarize the neighboring lattice. As a consequence, the samples exbibit NIR-shielding properties due to the

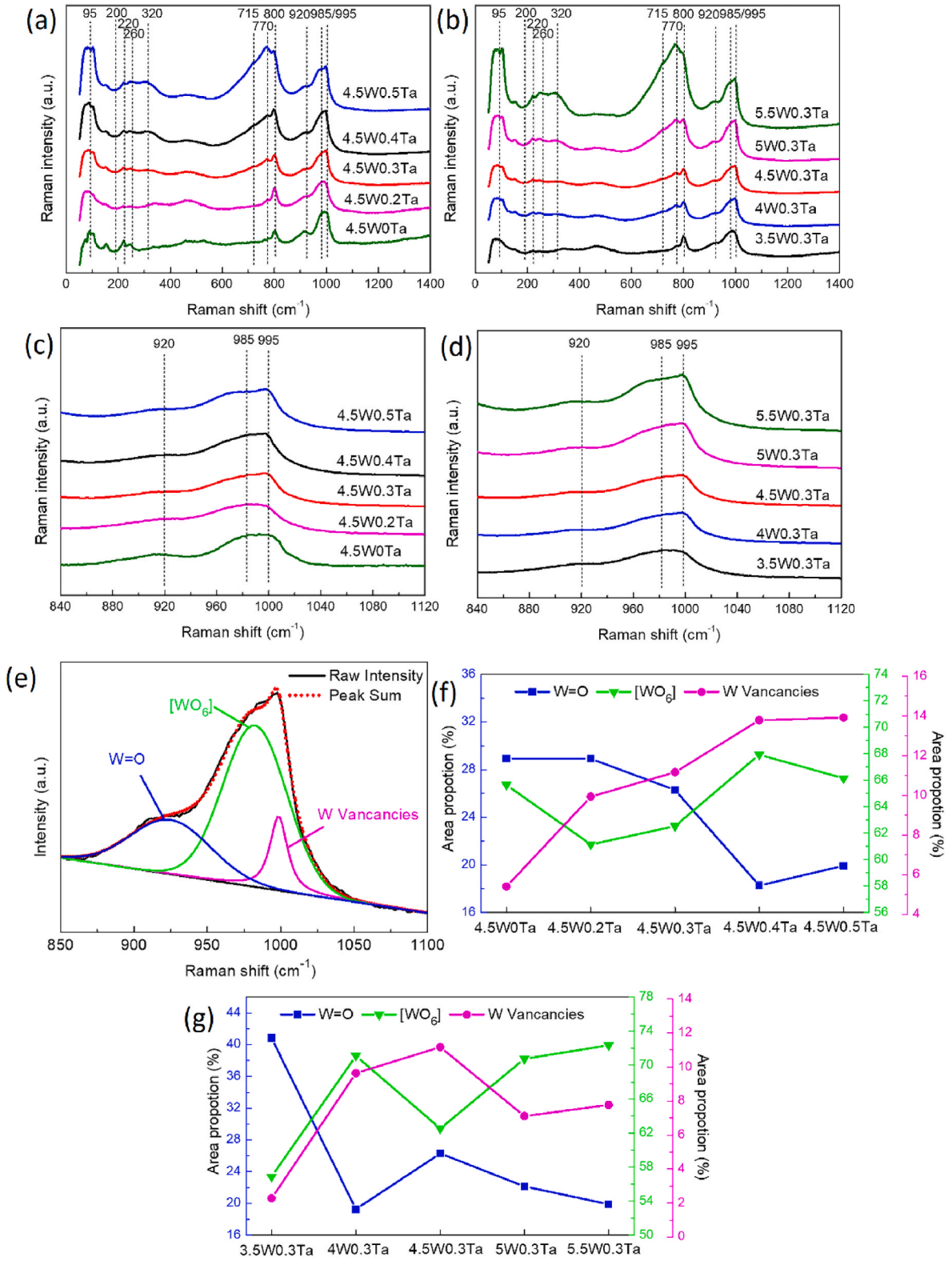

Fig. 5. Raman spectra of the samples (a, c) with different Ta_2O_5 concentration and (b, d) with different H_2WO_4 concentration. (e) Deconvolution of a Raman peak of sample 4.5W0.3Ta. The area proportions from deconvolution of a Raman peak of samples with different (f)Ta_2O_5 and (g) H_2WO_4 concentrations.

polarons-induced LSPR effect [22].

Fig. 5(a and b) show the Raman spectra of the samples prepared using varying Ta_2O_5 and H_2WO_4 contents in the raw materials. The Raman peaks in the range of 95–200 cm^{-1} can be assigned to the vibrational modes of tungsten-oxygen polyhedral lattice, and the Raman peak centered at ~220 cm^{-1} can be assigned to W–O–W stretching vibrations [39]. The two Raman peaks centered at ~260 cm^{-1} and ~320 cm^{-1} can be assigned to O–W–O bending vibrations [40]. In addition, the two Raman peaks centered at ~715 cm^{-1} and ~800 cm^{-1} can be assigned to the O–W–O stretching vibrations in crystalline WO_3 [39,41],

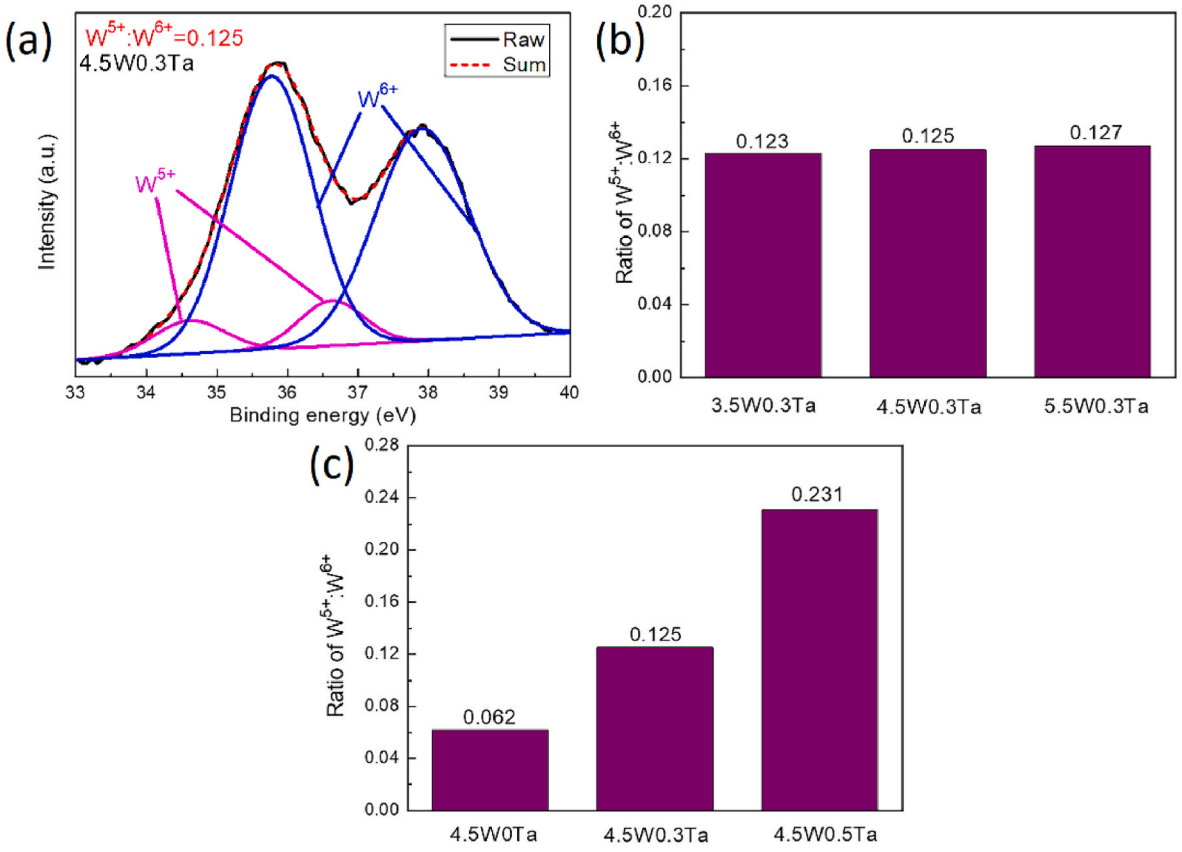

Fig. 6. (a) The W 4f XPS spectra of 4.5W0.3Ta sample and its fitting result. The W^{5+}/W^{6+} ratio of the samples (b) as a function of Ta_2O_5 concentration and (c) H_2WO_4 concentration.

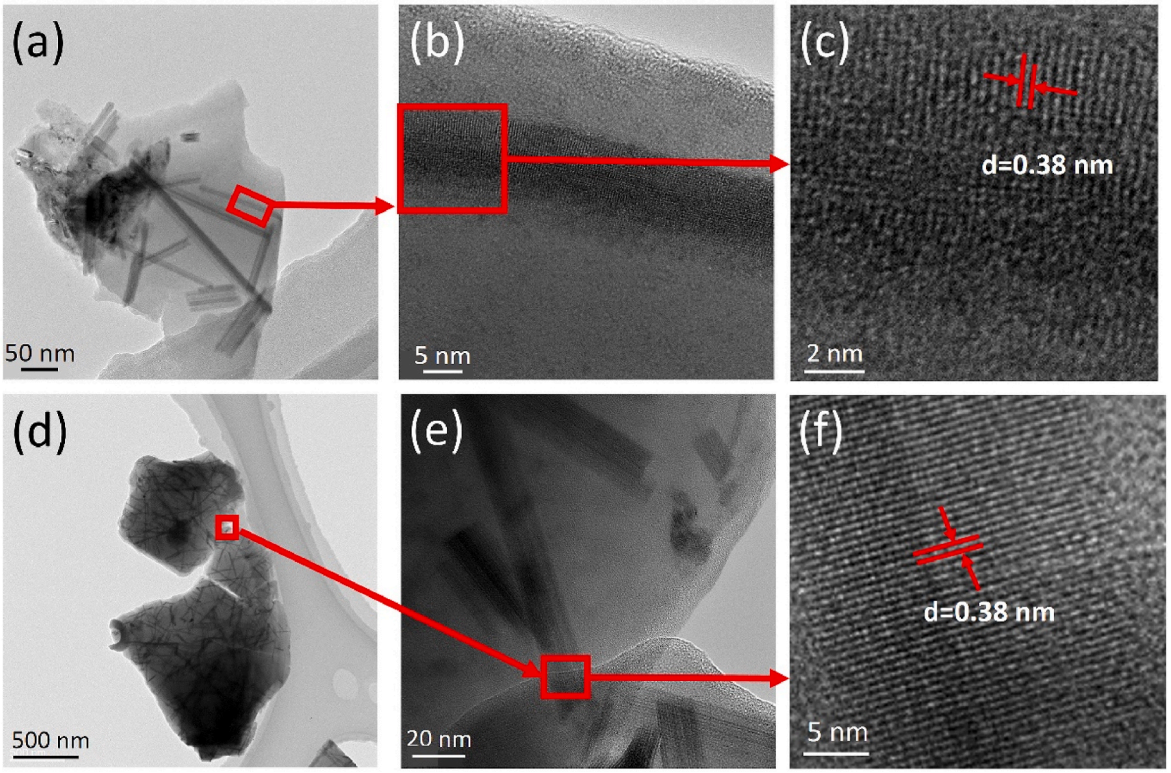

Fig. 7. TEM images under (a) low and (b) high magnifications and (c) HRTEM image of sample 4.5W0.5Ta. TEM images under (d) low and (e) high magnifications and (f) HRTEM image of sample 4.5W0.5Ta–C.

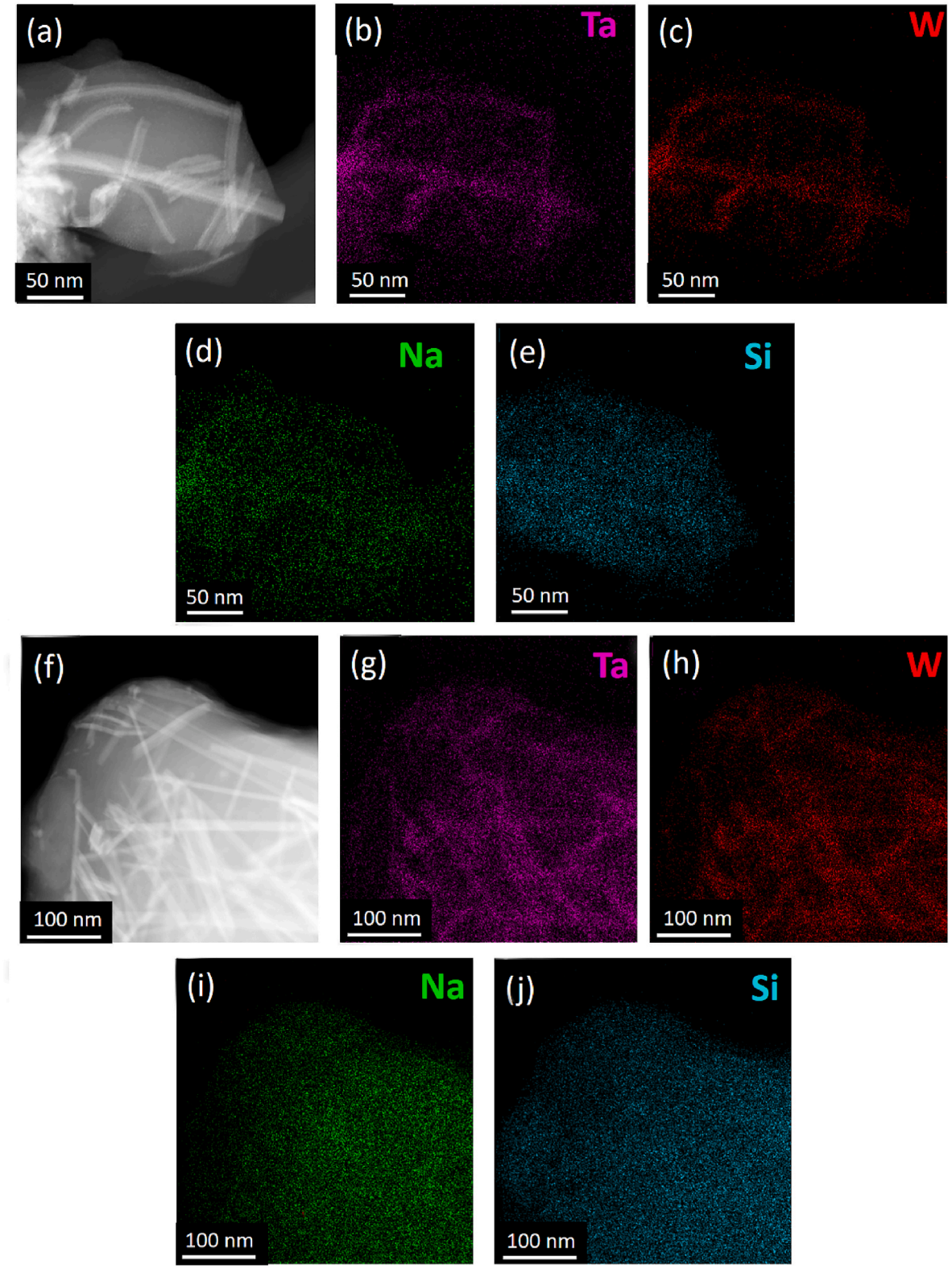

Fig. 8. (a) TEM image and (b–e) EDS mapping of the 4.5W0.5Ta sample. (f) TEM image and (g–j) EDS mapping of 4.5W0.5Ta–C sample.

and the peak intensity enhances with increasing content of H_2WO_4 and Ta_2O_5. This is because the degree of crystallization and concentration of $Ta_{0.3}W_{0.7}O_{2.85}$ nanocrystals increase with increasing content of H_2WO_4 and Ta_2O_5, based on XRD results (Fig. 4(a) and (b)). Moreover, the two Raman peaks centered at ~715 cm^{-1} and ~800 cm^{-1} in samples 5W0.3Ta, 5.5W0.3Ta, 4.5W0.4Ta and 4.5W0.5Ta are significantly stronger than in the other samples, in agreement with the presence of weak XRD diffraction peak at 47.8° in these four samples (Fig. 4(a) and (b)). Combining these Raman and XRD results, it can be concluded that these four samples contain larger amount of $Ta_{0.3}W_{0.7}O_{2.85}$ nanocrystals than in other samples. Similarly, the Raman peak centered at ~770 cm^{-1} can be assigned to the [TaO_6] octahedral structure in the

$Ta_{0.3}W_{0.7}O_{2.85}$ crystal, and the peak intensity raises with increasing content of H_2WO_4 and Ta_2O_5 [42]. The Raman peak centered at ~920 cm^{-1} can be assigned to a W═O terminal bond, but this terminal bond does not correlate with the coordination number of W atoms [43,44]. The Raman peak centered at ~985 cm^{-1} is attributed to the corner sharing [WO_6] octahedra, in both $Na_5W_{14}O_{44}$ and $Ta_{0.3}W_{0.7}O_{2.85}$ structures [45–47]. The intensity of this Raman peak increases with increasing H_2WO_4 content but is not obviously influenced by the Ta_2O_5 content. Raman peak centered at 995 cm^{-1} is assigned to the terminal bond W═O, which is related to W vacancies due to the substitution of W atoms by Ta atoms [48]. The [TaO_6] octahedra are present in the $Ta_{0.3}W_{0.7}O_{2.85}$ functional nanocrystals, therefore the Raman peak centered at 995 cm^{-1} becomes sharper with increasing Ta_2O_5 and/or H_2WO_4 content as shown in Fig. 5(a–d). The deconvoluted Raman peak in sample 4.5W0.3Ta is shown in Fig. 5(e) and the proportions of Raman peak deconvolution area are shown in Fig. 5(f) and (g). Area proportions of the peaks centered at ~920 cm^{-1}, ~985 cm^{-1}, and ~995 cm^{-1} can be used to infer the proportions of terminal bond W═O, [WO_6], and W vacancies in the samples, respectively. Fig. 5(f) shows increasing proportion of W vacancies with increasing concentration of Ta_2O_5, while Fig. 5(g) shows the maximum proportion of W vacancies in sample 4.5W0.3Ta produced using 4.5 mol% H_2WO_4. Therefore, the content of all tungsten oxides ($Ta_{0.3}W_{0.7}O_{2.85}$ and $Na_5W_{14}O_{44}$ in Fig. 4(c)) increases with increasing content of H_2WO_4 or Ta_2O_5, but Ta_2O_5 plays a more important role in the formation of $Ta_{0.3}W_{0.7}O_{2.85}$, which is further demonstrated in the subsequent XPS test results.

Fig. 6(a) shows the W 4f XPS spectrum of sample 4.5W0.3Ta. The spectrum can be deconvoluted into four peaks, corresponding to W^{5+} or W^{6+}. The two peaks centered at 34.6 eV and 36.7 eV can be assigned to W^{5+}, while the other two peaks centered at 37.8 eV and 35.7 eV can be assigned to W^{6+} [49,50]. The peak areas were obtained based on peak deconvolutions of the W^{5+} and W^{6+} peaks, and the peak area ratio (R), W^{5+}/W^{6+}, was used to indicate the relative abundance of W^{5+} and W^{6+} in the sample. The same XPS data processing was applied to the other samples and the obtained W^{5+}/W^{6+} ratios are presented in Fig. 6(b) and (c). Fig. 6(c) shows that R increases from 0.062 to 0.231 as the Ta_2O_5 content increases. This is because the increasing substitution of W^{6+} with Ta^{5+} in the WO_3 crystal structure forms more $Ta_{0.3}W_{0.7}O_{2.85}$ with oxygen vacancies, changing the surrounding chemical environment of W. This result agrees with reported work showing that Ta^{5+} doping leads to the formation of W^{5+} in Ta^{5+}-doped hexagonal WO_3 nanowires and cesium tungsten bronze [51,52]. The increase in W^{5+}/W^{6+} ratio with increasing Ta_2O_5 content agrees with the increase in molar proportion between the functional nanocrystal $Ta_{0.3}W_{0.7}O_{2.85}$ and $Na_5W_{14}O_{44}$, leading to enhanced NIR-shielding properties shown in Fig. 1(a). Additionally, Fig. 6(b) shows that increasing H_2WO_4 content has almost no effect on R, yet the transmission spectra indicate the enhanced NIR absorption with increasing H_2WO_4 content (Fig. 2(b)). This indicates that the total amount of functional nanocrystalline $Ta_{0.3}W_{0.7}O_{2.85}$ and $Na_5W_{14}O_{44}$ increases with increasing concentration of H_2WO_4, while the R of all tungsten oxides in the samples (Fig. 6(b)) remain almost unchanged. Like Raman, these XPS results suggest that Ta_2O_5 plays a more critical role than H_2WO_4 in the formation of $Ta_{0.3}W_{0.7}O_{2.85}$ functional units in the as-prepared glass-ceramic samples.

Fig. 7 shows the TEM and HRTEM images of samples 4.5W0.5Ta and 4.5W0.5Ta–C. Fig. 7(a) and (b) show that sample 4.5W0.5Ta contains fibrous nanocrystals with length of up to 200 nm and width of tens of nanometers. Fig. 7(d) and (e) show that after heat treatment, more and longer (up to 500 nm) fibrous nanocrystals are present in sample 4.5W0.5Ta–C, suggesting that heat treatment favors the formation and growth of functional phase nanocrystals. Furthermore, the HRTEM images in Fig. 7(c) and (f) show a d-spacing of 0.38 nm in the lattice of the fibrous nanocrystals. This d-spacing agrees with the {1 0 0} lattice planes of $Ta_{0.3}W_{0.7}O_{2.85}$ nanocrystals (PDF:45–0116). This d-spacing also agrees with the XRD patterns of samples 4.5W0.5Ta and 4.5W0.5Ta–C, where a strong (1 0 0) diffraction peak was present (Fig. 4 (a) and (c)). In the HRTEM image, the nanocrystals in sample 4.5W0.5Ta show some lattice distortion (Fig. 7(c)), while the lattice in sample 4.5W0.5Ta–C is clearer and well aligned (Fig. 7(f)), indicating that the heat treatment improved the crystallinity of the functional nanocrystal $Ta_{a0.3}W_{0.7}O_{2.85}$. Based on these TEM and HRTEM results, it can be concluded that the nanoscale fibrous nanocrystals $Ta_{0.3}W_{0.7}O_{2.85}$ are dispersed in the glass matrix.

Fig. 8 shows EDS elemental distributions in samples 4.5W0.5Ta and 4.5W0.5Ta–C. Fig. 8(b–e) and (g-j) show EDS mapping in the areas shown in Fig. 8(a) and (f), respectively. The fibrous nanocrystals are enriched in Ta and W (Fig. 8(b,c,g,h)), in agreement with the composition of the $Ta_{0.3}W_{0.7}O_{2.85}$ nanocrystals; while the homogeneous distribution of Na and Si indicate the homogeneous composition of the bulk borosilicate glass matrix (Fig. 8(d, e, i, j)). Combining XRD, HRTEM, and EDS results, it can be concluded that the nanoscale fibrous nanocrystals are $Ta_{0.3}W_{0.7}O_{2.85}$.

4. Conclusions

In this work, NIR-shielding glass-ceramics were fabricated by a facile melt-quenching technique. The NIR-shielding performance is due to the formation of functional $Ta_{0.3}W_{0.7}O_{2.85}$ nanocrystals in the borosilicate glass matrix and can be tuned by adjusting the concentration of H_2WO_4 and Ta_2O_5 in the raw materials. The optimized glass ceramic sample fabricated with 4.5 mol% H_2WO_4 and 0.3 mol% Ta_2O_5 exhibits an excellent NIR-shielding ability (ΔT = 68.9%) and a high visible light transmittance (T_{max} = 74.4%), suitable for applications in NIR-shielding energy-saving windows. Based on simulation tests, the optimized glass ceramic sample has much better thermal insulation ability than soda lime glass and ITO glass, and better visible light transmittance than CWO film glass. The formation of $Ta_{0.3}W_{0.7}O_{2.85}$ functional nanocrystals were confirmed by XRD, Raman, TEM, HRTEM, and EDS characterization and the NIR-shielding property can be attributed to the presence of oxygen vacancies in $Ta_{0.3}W_{0.7}O_{2.85}$ due to the substitution of W with Ta in the crystal lattice. This study provides a chemical tuning method for the optimization of defective tungsten oxide nanocrystals doping in bulk glass matrix for the fabrication of NIR-shielding energy-saving window materials.

Declaration of competing interest

The authors declare that they have no known competing financial interests or personal relationships that could have appeared to influence the work reported in this paper.

Acknowledgments

This work is supported by the National Natural Science Foundation of China (No. 52072231), the Chinese - Ukrainian International Exchange Project for the Period of 2022–2023 of Ministry of Science and Technology of China, the Presidential Foundation of the China Academy of Engineering Physics (YZJJLX2019011), and the Engineering and Physical Sciences Research Council, UK (grant number EP/S030786/1).

References

[1] S. Leitner, R. Hood-Nowotny, A. Watzinger, Successive and automated stable isotope analysis of CO_2, CH_4 and N_2O paving the way for unmanned aerial vehicle-based sampling, Rapid Commun. Mass Spectrom. 34 (2020), e8929, https://doi.org/10.1002/rcm.8929. -e8929.

[2] A. Ghosh, B. Norton, Advances in switchable and highly insulating autonomous (self-powered) glazing systems for adaptive low energy buildings, Renew. Energy 126 (2018) 1003–1031, https://doi.org/10.1016/j.renene.2018.04.038.

[3] Y. Yıldız, Z.D. Arsan, Identification of the building parameters that influence heating and cooling energy loads for apartment buildings in hot-humid climates, Energy 36 (2011) 4287–4296, https://doi.org/10.1016/j.energy.2011.04.013.

[4] Y. Ke, J. Chen, G. Lin, S. Wang, Y. Zhou, J. Yin, P.S. Lee, Y. Long, Smart windows: electro-, Thermo-, mechano-, photochromics, and beyond, Adv. Energy Mater. 9 (2019), 1902066, https://doi.org/10.1002/aenm.201902066.

[5] D. Wang, X. Wu, Q. Gao, Novel energy-saving window coating based on F doped TiO_2 nanocrystals with enhanced NIR shielding performance, Ceram. Int. 47 (2021) 28557–28565, https://doi.org/10.1016/j.ceramint.2021.07.013.

[6] S.D. Rezaei, S. Shannigrahi, S. Ramakrishna, A review of conventional, advanced, and smart glazing technologies and materials for improving indoor environment, Sol. Energy Mater. Sol. Cells 159 (2017) 26–51, https://doi.org/10.1016/j.solmat.2016.08.026.

[7] M. Li, S. Magdassi, Y. Gao, Y. Long, Hydrothermal synthesis of VO_2 polymorphs: advantages, challenges and prospects for the application of energy efficient smart windows, Small 13 (2017), 1701147, https://doi.org/10.1002/smll.201701147.

[8] Y. Gao, S. Wang, H. Luo, L. Dai, C. Cao, Y. Liu, Z. Chen, M. Kanehira, Enhanced chemical stability of VO_2 nanoparticles by the formation of SiO_2/VO_2 core/shell structures and the application to transparent and flexible VO_2-based composite foils with excellent thermochromic properties for solar heat control, Energy Environ. Sci. 5 (2012) 6104–6110, https://doi.org/10.1039/c2ee02803d.

[9] P. Pattathil, R. Giannuzzi, M. Manca, Self-powered NIR-selective dynamic windows based on broad tuning of the localized surface plasmon resonance in mesoporous ITO electrodes, Nano Energy 30 (2016) 242–251, https://doi.org/10.1016/j.nanoen.2016.10.013.

[10] J. Shao, H. Shen, K. Gao, X. Huo, J. Saddique, X. Wang, W. Meng, UV- and NIR-blocking properties of ZnO/ATO bilayer films prepared by RF magnetron sputtering, Opt. Mater. 118 (2021), 111287, https://doi.org/10.1016/j.optmat.2021.111287.

[11] H. Zhang, J. Liu, F. Shi, S. Jiang, X. Song, M. Wasim, X. Song, J. Ma, Controlling the growth of hexagonal Cs_xWO_3 nanorods by Li^+-doping to further improve its near infrared shielding performance, Sol. Energy Mater. Sol. Cells 238 (2022), 111612, https://doi.org/10.1016/j.solmat.2022.111612.

[12] G. Yang, D. Hu, C. Yang, Y. Qi, B. Liu, H. Chen, L. Zhang, Y. Cui, X. Yao, V. Takats, Alkali metal tungsten bronze-doped energy-saving glasses for near-infrared shielding applications, Ceram. Int. 47 (2021) 31122–31129, https://doi.org/10.1016/j.ceramint.2021.07.286.

[13] L. Chao, L. Bao, W. Wei, O. Tegus, A review of recent advances in synthesis, characterization and NIR shielding property of nanocrystalline rare-earth hexaborides and tungsten bronzes, Sol. Energy 190 (2019) 10–27, https://doi.org/10.1016/j.solener.2019.07.087.

[14] S. Wang, T. Jiang, Y. Meng, R. Yang, G. Tan, Y. Long, Scalable thermochromic smart windows with passive radiative cooling regulation, Science 374 (2021) 1501–1504, https://doi.org/10.1126/science.abg0291.

[15] S. Wang, Y. Zhou, T. Jiang, R. Yang, G. Tan, Y. Long, Thermochromic smart windows with highly regulated radiative cooling and solar transmission, Nano Energy 89 (2021), 106440, https://doi.org/10.1016/j.nanoen.2021.106440.

[16] K. Adachi, Y. Ota, H. Tanaka, M. Okada, N. Oshimura, A. Tofuku, Chromatic instabilities in cesium-doped tungsten bronze nanoparticles, J. Appl. Phys. 114 (2013), 194304, https://doi.org/10.1063/1.4831950.

[17] G. Yang, Y. Qi, D. Hu, H. Wang, H. Chen, L. Zhang, C. Cao, B. Liu, F. Xia, Y. Gao, Sodium tungsten bronze (Na_xWO_3)-doped near-infrared-shielding bulk glasses for energy-saving applications, J. Mater. Sci. Technol. 89 (2021) 150–157, https://doi.org/10.1016/j.jmst.2020.12.082.

[18] Y. Chen, X. Zeng, Y. Zhou, R. Li, H. Yao, X. Cao, P. Jin, Core-shell structured Cs_xWO_3@ZnO with excellent stability and high performance on near-infrared shielding, Ceram. Int. 44 (2018) 2738–2744, https://doi.org/10.1016/j.ceramint.2017.11.004.

[19] H. Takeda, K. Adachi, Near infrared absorption of tungsten oxide nanoparticle dispersions, J. Am. Ceram. Soc. 90 (2007) 4059–4061, https://doi.org/10.1111/j.1551-2916.2007.02065.x.

[20] C. Guo, S. Yin, T. Sato, Effects of crystallization atmospheres on the near-infrared absorbtion and electroconductive properties of tungsten bronze type M_xWO_3 (M = Na, K), J. Am. Ceram. Soc. 95 (2012) 1634–1639, https://doi.org/10.1111/j.1551-2916.2011.05039.x.

[21] C. Guo, S. Yin, M. Yan, M. Kobayashi, M. Kakihana, T. Sato, Morphology-controlled synthesis of $W_{18}O_{49}$ nanostructures and their near-infrared absorption properties, Inorg. Chem. 51 (2012) 4763–4771, https://doi.org/10.1021/ic300049j.

[22] H. Quan, Y. Gao, W. Wang, Tungsten oxide-based visible light-driven photocatalysts: crystal and electronic structures and strategies for photocatalytic efficiency enhancement, Inorg. Chem. Front. 7 (2020) 817–838, https://doi.org/10.1039/C9QI01516G.

[23] K.R. Locherer, I.P. Swainson, E.K.H. Salje, Transition to a new tetragonal phase of WO_3: crystal structure and distortion parameters, J. Phys. Condens. Matter 11 (1999) 4143–4156, https://doi.org/10.1088/0953-8984/11/21/303.

[24] C. Guo, S. Yin, Q. Dong, T. Sato, The near infrared absorption properties of $W_{18}O_{49}$, RSC Adv. 2 (2012) 5041–5043, https://doi.org/10.1039/C2RA01366E.

[25] C.-M. Wu, S. Naseem, M.-H. Chou, J.-H. Wang, Y.-Q. Jian, Recent advances in tungsten-oxide-based materials and their applications, Front. Mater. 6 (2019) 49, https://doi.org/10.3389/fmats.2019.00049.

[26] W. Mu, X. Xie, X. Li, R. Zhang, Q. Yu, K. Lv, H. Wei, Y. Jian, Characterizations of Nb-doped WO_3 nanomaterials and their enhanced photocatalytic performance, RSC Adv. 4 (2014) 36064–36070, https://doi.org/10.1039/C4RA04080E.

[27] X.C. Song, E. Yang, G. Liu, Y. Zhang, Z.S. Liu, H.F. Chen, Y. Wang, Preparation and photocatalytic activity of Mo-doped WO_3 nanowires, J. Nanoparticle Res. 12 (2010) 2813–2819, https://doi.org/10.1007/s11051-010-9859-8.

[28] A. Enesca, A. Duta, J. Schoonman, Influence of tantalum dopant ions (Ta^{5+}) on the efficiency of the tungsten trioxide photoelectrode, Phys. Status Solidi A 205 (2008) 2038–2041, https://doi.org/10.1002/pssa.200778858.

[29] C. Feng, S. Wang, B. Geng, Ti(iv) doped WO_3 nanocuboids: fabrication and enhanced visible-light-driven photocatalytic performance, Nanoscale 3 (2011) 3695–3699, https://doi.org/10.1039/C1NR10460H.

[30] X.F. Cheng, W.H. Leng, D.P. Liu, J.Q. Zhang, C.N. Cao, Enhanced photoelectrocatalytic performance of Zn-doped WO_3 photocatalysts for nitrite ions degradation under visible light, Chemosphere 68 (2007) 1976–1984, https://doi.org/10.1016/j.chemosphere.2007.02.010.

[31] T. Kudo, A. Ishikawa, H. Okamoto, K. Miyauchi, Cubic ReO_3-type $W_{1-x}Ta_xO_{3-x/2}$ and $W_{1-x}Nb_xO_{3-x/2}$, J. Solid State Chem. 77 (1988) 412–415, https://doi.org/10.1016/0022-4596(88)90266-6.

[32] D. Yang, Structural and electrochromic characterizations of pulsed laser deposited $Ta_xW_{1-x}O_{3-x/2}$ films, J. Vac. Sci. Technol., A 24 (2006) 1128–1135, https://doi.org/10.1116/1.2209652.

[33] Y. Yao, L. Zhang, Z. Chen, C. Cao, Y. Gao, H. Luo, Synthesis of Cs_xWO_3 nanoparticles and their NIR shielding properties, Ceram. Int. 44 (2018) 13469–13475, https://doi.org/10.1016/j.ceramint.2018.04.158.

[34] X. Song, J. Liu, F. Shi, C. Fan, S. Ran, H. Zhang, Z. Zou, Facile fabrication of $K_mCs_nWO_3$ with greatly improved near-infrared shielding efficiency based on W^{5+}-induced small polaron and local surface plasmon resonance (LSPR) modulation, Sol. Energy Mater. Sol. Cells 218 (2020), 110769, https://doi.org/10.1016/j.solmat.2020.110769.

[35] G. Yang, C. Yang, F. Xia, D. Hu, J. Brugger, B.E. Etschmann, J. Hamilton, H. Chen, Y. Gao, Energy-saving glasses based on sodium tungsten bronze-like ($Na_5W_{14}O_{44}$) functional units: facile synthesis, NIR-shielding performance, and formation mechanism, Ceram. Int. 48 (2022) 21141–21150, https://doi.org/10.1016/j.ceramint.2022.04.005.

[36] G. Yang, D. Hu, F. Xia, C. Yang, Y. Liu, X. He, Y. Shpotyuk, H. Chen, Y. Gao, Doping sodium tungsten bronze-like ($Na_5W_{14}O_{44}$) near-infrared shielding functional units in bulk borosilicate glasses for energy-saving window applications, ACS Appl. Mater. Interfaces 14 (2022) 32206–32217, https://doi.org/10.1021/acsami.2c03640.

[37] Y. Yao, Z. Chen, W. Wei, P. Zhang, Y. Zhu, Q. Zhao, K. Lv, X. Liu, Y. Gao, $Cs_{0.32}WO_3$/PMMA nanocomposite via in-situ polymerization for energy saving windows, Sol. Energy Mater. Sol. Cells 215 (2020), 110656, https://doi.org/10.1016/j.solmat.2020.110656.

[38] D. Yang, L. Xue, Structures and electrochromic properties of $Ta_{0.3}W_{0.7}O_l$ thin films deposited by pulsed laser ablation, Thin Solid Films 494 (2006) 28–32, https://doi.org/10.1016/j.tsf.2005.07.169.

[39] K. Thummavichai, L. Trimby, N. Wang, C.D. Wright, Y. Xia, Y. Zhu, Low temperature annealing improves the electrochromic and degradation behavior of tungsten oxide (WO_x) thin films, J. Phys. Chem. C 121 (2017) 20498–20506, https://doi.org/10.1021/acs.jpcc.7b06300.

[40] B. Ingham, S.V. Chong, J.L. Tallon, Layered tungsten oxide-based Organic−Inorganic hybrid materials: an infrared and Raman study, J. Phys. Chem. B 109 (2005) 4936–4940, https://doi.org/10.1021/jp045066l.

[41] V.S. Kavitha, S. Suresh, S.R. Chalana, V.P. Mahadevan Pillai, Luminescent Ta doped WO_3 thin films as a probable candidate for excitonic solar cell applications, Appl. Surf. Sci. 466 (2019) 289–300, https://doi.org/10.1016/j.apsusc.2018.10.007.

[42] L. Cordeiro, R.M. Silva, G.M. de Pietro, C. Pereira, E.A. Ferreira, S.J.L. Ribeiro, Y. Messaddeq, F.C. Cassanjes, G. Poirier, Thermal and structural properties of tantalum alkali-phosphate glasses, J. Non-Cryst. Solids 402 (2014) 44–48, https://doi.org/10.1016/j.jnoncrysol.2014.05.015.

[43] G. Poirier, Y. Messaddeq, S.J.L. Ribeiro, M. Poulain, Structural study of tungstate fluorophosphate glasses by Raman and X-ray absorption spectroscopy, J. Solid State Chem. 178 (2005) 1533–1538, https://doi.org/10.1016/j.jssc.2004.10.032.

[44] T. Sekiya, N. Mochida, S. Ogawa, Structural study of WO_3-TeO_2 glasses, J. Non-Cryst. Solids 176 (1994) 105–115, https://doi.org/10.1016/0022-3093(94)90067-1.

[45] J. Wang, J.L. You, A.A. Sobol, L.M. Lu, M. Wang, J. Wu, X.M. Lv, S.M. Wan, In-situ high temperature Raman spectroscopic study on the structural evolution of $Na_2W_2O_7$ from the crystalline to molten states, J. Raman Spectrosc. 48 (2017) 298–304, https://doi.org/10.1002/jrs.5036.

[46] S.T. Triantafyllou, P.C. Christidis, Triclinic sodium tungsten oxide, $Na_5W_{14}O_{44}$, Acta Crystallogr. C 55 (1999) 838–841, https://doi.org/10.1002/chin.199938002.

[47] M. Couzi, P. Rocquet, J.P. Chaminade, J. Ravez, Raman scattering and group-theoretical studies of the paraelectric-ferroelectric phase transition in the chiolite-type-crystal $Na_5W_3O_9F_5$, Ferroelectrics 80 (1988) 113–116, https://doi.org/10.1080/00150198808223272.

[48] M. Okada, K. Ono, S. Yoshio, H. Fukuyama, K. Adachi, Oxygen vacancies and pseudo Jahn-Teller destabilization in cesium-doped hexagonal tungsten bronzes, J. Am. Ceram. Soc. 102 (2019) 5386–5400, https://doi.org/10.1111/jace.16414.

[49] Y. Li, X. Wu, J. Li, K. Wang, G. Zhang, Z-scheme g-C_3N_4@Cs_xWO_3 heterostructure as smart window coating for UV isolating, Vis penetrating, NIR shielding and full spectrum photocatalytic decomposing VOCs, Appl. Catal., B 229 (2018) 218–226, https://doi.org/10.1016/j.apcatb.2018.02.024.

[50] Y. Chang, Z. Wang, Y.-e. Shi, X. Ma, L. Ma, Y. Zhang, J. Zhan, Hydrophobic $W_{18}O_{49}$ mesocrystal on hydrophilic PTFE membrane as an efficient solar steam generation device under one sun, J. Mater. Chem. 6 (2018) 10939–10946, https://doi.org/10.1039/C8TA02700E.

[51] X. Xie, W. Mu, X. Li, H. Wei, Y. Jian, Q. Yu, R. Zhang, K. Lv, H. Tang, S. Luo, Incorporation of tantalum ions enhances the electrocatalytic activity of hexagonal WO_3 nanowires for hydrogen evolution reaction, Electrochim. Acta 134 (2014) 201–208, https://doi.org/10.1016/j.electacta.2014.04.122.

[52] Y. Hua, C. Huang, L. Li, T. Zhou, L. Yan, X. Yue, W. Lv, Q. Qiu, Mechanism of $Cs_{0.33}Ta_xW_{1-x}O_3$ in improving the optical property, Mater. Chem. Phys. 250 (2020), 122992, https://doi.org/10.1016/j.matchemphys.2020.122992.